Using Geologic and Geodetic Analyses to Define the Location, Slip Rate, and Geometry of Off Fault Deformation, Hidden Spring Fault Zone, Southern California

Rebekah Riemann[1], James Evans[1], Susanne Jänecke[1], Andrea Donnellan[2], Jay Parker[2]

Abstract

A strain deficit of about 10 mm/yr exists across the San Andreas Fault system on the boundary between the North American and Pacific plates. We investigate the role of the Hidden Spring Fault Zone, east of the Salton Sea in Southern California, and related structures in accommodating some of this slip. We compile data from historic and current aerial and satellite imagery, coupled with UAVSAR and LiDAR data have allowed us to identify and map hundreds of new fault segments in the region. Where possible, we correlate some of these data with geologic evidence for the faults. These data emphasize the orientations and potential fault linkages that are vital for a kinematic analysis of the Hidden Spring Fault Zone and in creating a baseline analysis of deformation in a region where large seismic ruptures are likely to occur.

Introduction

The San Andreas Fault (SAF) poses the largest long-term seismic risk in the continental United states (Peterson, 2014) and when it ruptures will affect millions of people in the San Diego and Los Angeles metropolitan areas. Thus, there is a large focus to understand how this fault has behaved and will behave before, during, and after a large earthquake. The current worst-case scenario for a SAF event is that an earthquake will nucleate on the southern strand of the San Andreas Fault (SSAF) as far south as Bombay Beach (Field et al., 2013; Jänecke et al., 2018) and propagate northward towards the Los Angeles Basin (Figure 1), impacting up to 30 million residents.

Motivation

The SAF is a transform fault on the boundary between the North American and Pacific plates. Despite a geodetically derived slip rate between these two plates of ~48.5 mm/yr, only ~22 mm/yr is accommodated on the SAF itself (DeMets et al., 2010; Evans et al., 2015; Fialko 2006; Lindsey et al., 2014; Spinler et al., 2010), meaning the remaining strain must be accommodated elsewhere. Many models, using geodetically determined motions, only consider faults west of the SAF in their strain budget, such as the Elsinore Fault (EF) and the San Jacinto fault (SJF), or assume geologically unrealistic block models of the region (Evans et al., 2015). If we consider the entire tectonic slip budget for the plate boundary zone to be 48.5 mm/yr, at its largest estimates the SSAF is thought to accommodate between 12 and 25 mm/yr (Evans et al., 2015; Fialko, 2006; Lindsey and Fialko, 2013; Lundgren et al., 2009; Rockwell et al., 2016; Spinler et al., 2010; Tong and Sandwell, 2013). The SJF accommodates a significant amount, between 9 and 21 mm/yr, of plate motion (Evans et al., 2015; Jänecke et al., 2010; Lindsey et al., 2014; Lisowski et al., 1991), which may reflect a deficit of tectonic slip as high as 10 mm/yr not accounted for on the EF and SSAF. It is, therefore, imperative that we determine where and how this remainder of plate boundary slip is accommodated. Some geodetic studies suggest up to 10 mm/yr of this right-lateral motion may be accommodated on the Hidden Spring Fault (HSF) although this slip does not coincide with its modeled trace.

[1] Department of Geoscience, Utah State University, 4505 Old Main Hill, Logan, UT 84322
[2] Jet Propulsion Laboratory California Institute of Technology, National Aeronautics and Space Administration, Pasadena, CA 91109

In addition to deciphering how much slip is accommodated on these eastern faults, it is necessary we understand the nature of that slip. Faults can accommodate coseismic slip, and increasingly we have come to realize that many faults may also accommodate aseismic slip, or creep. If the total slip observed on a fault is ascribed to coseismic slip when the fault experiences aseismic creep, this would lead to overestimates of potential seismic hazards. Conversely, to assume the faults are experiencing aseismic slip, when the slip is predominately seismic and episodic, would lead to underestimates of seismic hazard, affecting building codes and infrastructure. Incorrectly asserting the nature of slip could negatively affect the 30 million people living in this region.

This study is, in part, motivated by how little is published on the HSF, the limited accuracy with which the HSF is mapped, the high slip rate inferred across the HSF in some models, and the setting of the area relative to the Eastern California Shear Zone (Donnellan et al., 2017). Current geodetic models show the right lateral plate motion east of the SSAF is not well constrained by current geologic data. In the Mojave Desert, slip rates obtained geologically reflect displacement ranging from 6 mm/yr to 8 mm/yr, yet geodetic estimates of displacement could be as high as 18 mm/yr (Thatcher et al., 2016; Evans et al., 2015, 2016, 2018). Some of this strain may be accommodated on a fault such as the HSF, although it is unlikely, based on the geomorphology of the area, that the entire 12 mm/yr is being accommodated on this fault. The geologic expression of the HSF is too limited for such high slip rates to be realistic. A more likely explanation for some of the missing tectonic slip is that it is accommodated on smaller and/or cryptic or hidden faults east of the SSAF, potentially along the proposed Hidden Spring Fault Zone (HSFZ), or that there is an incipient version of the highly sheared Durmid Ladder structure nearby (Jänecke et al., 2018). This would account for the geodetically predicted slip as well as resolving the limitations of geodesy.

We investigate the roles that the HSFZ and related structures east of the SSAF play in accommodating some of this missing slip. While the slip rate of the HSFZ may be significant, either

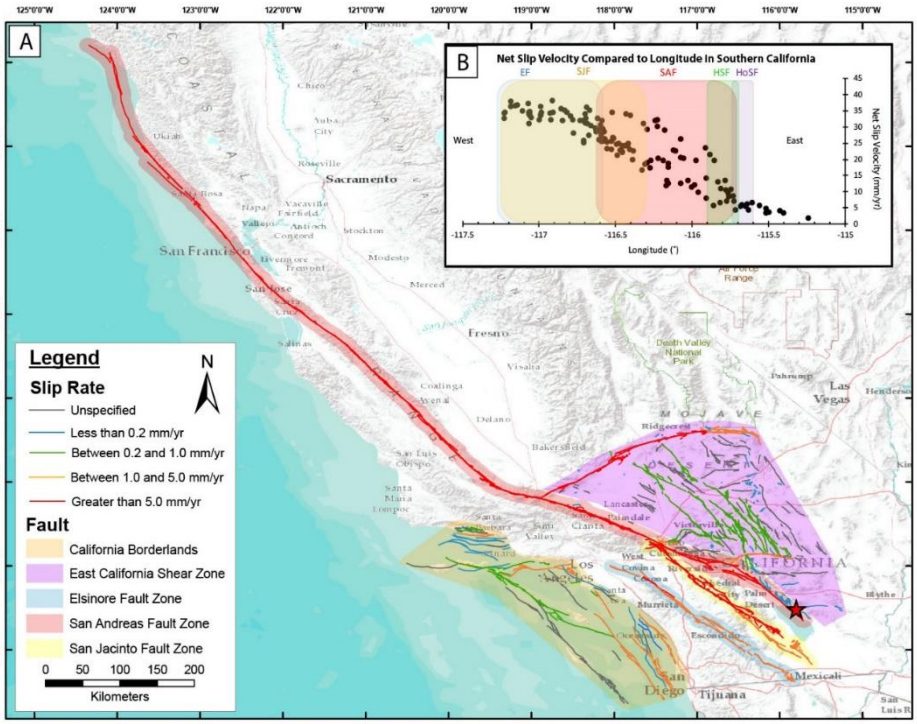

Figure 1. A. Map of California showing the pertinent fault zones. Fault locations have been sourced from the Quaternary Fault and Fold Database (USGS, 2006; Bryant, 2005) **B.** Net slip velocity as a function of longitude across Southern California between latitudes 33.8°N and 33.26°N. Slip velocities were measured relative to the Stable North American Reference Frame (Zheng and Shen, 2016; Sandwell and Wessel, 2018). Slip velocities between 5 and 15 mm/yr are indicated in the Hidden Spring Fault Zone. About 8 mm/yr probably occur offshore in the California Borderlands because the total plate motion is 48.4 mm/yr (Demets and Merkouriev, 2016).

5 or 12 mm/yr according to geodetic models (Evans et al., 2015, 2016: Jennings, 1994), the subtle geomorphic expression of the HSFZ does not appear to support such a high slip rate. One possible explanation for this discrepancy is that the HSFZ is a voluminous fault zone (discussed below; Cheng et al., 2018; Evans et al., 2018 SCEC Prop.; Jänecke et al., 2010, 2018; Polet et al, 2019) that accommodates slip on many, relatively smaller, faults. I test whether the HSFZ is a voluminous fault zone by improving the current fault mapping and deciphering the geometric and kinematic relationship between the HSFZ, nearby fault strands, and the SSAF. We combine the capabilities of Google Earth Pro and ArcMap (Google, 2020; ESRI, 2019) with available imagery and UAVSAR data to accomplish this goal.

Background

The Hidden Spring Fault as a Voluminous Fault Zone

Field studies (Jänecke and Thomann, current research; Evans, Moser, Bradbury, unpublished work; Moser, 2017) suggest that the HSFZ forms a ladder structure south of the projected intersection with the Salton Creek Fault, where it is up to 10 km wide (Figure 2), and accommodates an uncertain amount of tectonic slip from the SSAF. The northwest edge of the HSFZ is approximately six kilometers east of the SSAF and constitutes the eastern edge of the Mecca Hills (Dibblee, 1954). The fault zone can be traced from the Mecca Hills south to Salt Creek where the main trace of the HSF appears to die out. Instead, the right lateral Powerline Fault (PF) (Bryant, 2012; Babcock, 1974) on the northeast margin of the ladder structure, may take over as the largest master fault. Southward, the master fault steps left ~3 km onto the Hot Springs Fault (HoSF) (Figure 2) (Jänecke et al., 2018, Jennings, 1994; Bryant, 2012; McNabb et al., 2017). A small number of the faults associated with the greater HSFZ, east of its main trace, have been mapped at a range of scales in the last 70 years (Babcock, 1974; Bryant, 2012; Hays, 1957; Jänecke et al., 2018; McNabb, 2017; Markowski, 2016). Recent mapping by Jänecke's research group identified a possible active voluminous fault zone there, with evidence for creep and triggered slip on both northeast and northwest striking faults.

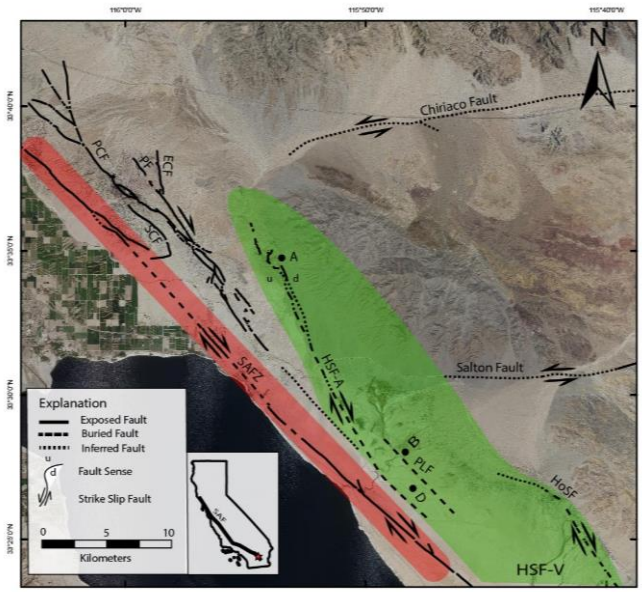

Figure 2. Faults proximal to the study area. Letters A, B and D refer to the locations of the images in Figure 4. The red shading indicates the approximate extent of the SAFZ and the green shading indicates the extent of the proposed HSF-V (Evans et al., proposal 2018). The inset map in this figure and all subsequent figures provides spatial context with the red star indicated the location of this study relative to the state of California (Bryant, 2005; CA dep. of Fish and Wildlife, 2016).

When we discuss the HSFZ as a voluminous fault zone we hypothesize that rather than a singular fault trace, or traditional fault zone, the HSFZ forms a ladder structure. The HSFZ would be characterized by two master right-lateral faults, HSF on its south west edge and another eastern fault such as the PLF or the HoSF. Between the two faults there is evidence for a series of cross faults or 'rungs' of the ladder, similar to the structures of the Brawley Seismic Zone (Jänecke et al., 2018; Hauksson, 2017; Markowski, 2016). If we consider the slip deficit in terms of the voluminous fault theory, twenty small faults each accommodating a reasonable 0.5 mm/yr of slip would account for the missing 10 mm/yr of slip. Dispersed strain observed in UAVSAR data, previously interpreted as noise,

may corroborate these predictions (Figure 3B; Donnellan, 2019 Pers. Comm.).

Seismic Risk

In relation to the SSAF, adjacent or cross faults such as the HSFZ can alter fault stresses enough to trigger a rupture given the right conditions (Fletcher et al., 2014; Jänecke et al., 2018; Kyriakopoulos et al., 2019; Lin & Stein, 2004) and current rupture models (Roten et al. ,2017) of fault zone plasticity don't consider the effects of faults east of the SSAF on rupture propagation. The existence of a high slip rate fault zone, like the HSFZ, could alter these forecasts, as could different geometries of the HSFZ. If the main trace of the HSF is hard linked to the SSAF, and an earthquake nucleates near Bombay Beach, as predicted or modeled, some slip could be distributed on the SAFZ and HSFZ and significantly attenuate by the time the energy reaches the LA Basin. In wide fault zones ground shaking can be reduced by as much as 70% (Roten et al., 2014, 2017). Alternatively, if the HSFZ is a voluminous fault zone there may be a reduction in the localization of deformation (Roten et al, 2014, 2017). Rather than an event on the HSF being localized to a narrow fault, the seismic energy may spread across a network of faults and fracture zones, possibly triggering additional events (Cheng et al., 2018). Understanding how and where a large earthquake on the SAF will nucleate and propagate is critical for creating accurate seismic hazard assessments in this region.

Geologic Setting

This region of the fault zone encompasses of the Coachella Valley segment of the SAF, which terminates in the southern Salton Sea at the Brawley Seismic Zone, as well as the SJF and EF (Dibblee, 1954; Fattaruso et al., 2016; McNabb et al., 2017; Jänecke et al., 2018; Tong et al., 2012, 2013). Since the late Miocene, transform tectonics have produced transtensional and transpressional features in this region (Axen and Fletcher, 1998; Dorsey et al., 2011; McNabb et al, 2017). All three of the currently active transform faults crosscut the once continuous West Salton Detachment Fault (WSDF), a low angle extensional fault, active through the early Pleistocene. The WSDF was deactivated ca. 1.1 -1.3 Ma following a major tectonic reorganization which initiated the SJF and the EF, as well as the Mecca Hills faults (Axen and Fletcher, 1998; Dorsey & Umhoefer, 2012; Jänecke et al., 2010; Kirby et al., 2007; Lutz, 2005; Lutz et al., 2006; Moser et al., 2018; Steely et al., 2009). This reorganization resulted in 25 km of relative plate motion across the SJF since its inception (Sharp, 1967). The termination of the WSDF and initiation of the SJF and EF resulted in a change from subsidence of the area to uplift of large areas within the basin, as well as the onset of tight folding (Dorsey & Umhoefer, 2012; Fattaruso et al., 2016; Jänecke et al., 2010; Steely et al., 2009; Kirby et al, 2007).

Locally the HSF offsets Pleistocene to Holocene alluvium and Lake Cahuilla deposits from the last ca. 1420 years (Babcock, 1969; Bryant, 2012; Crowell 1959; Hays, 1957; Jänecke

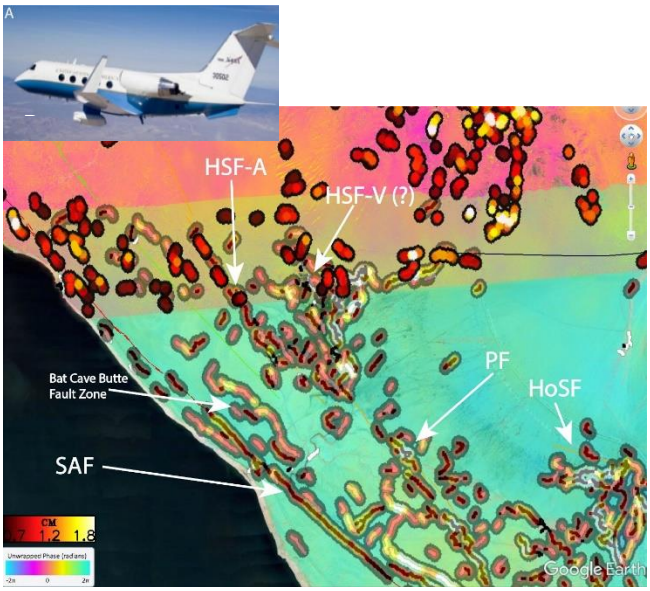

Figure 3. A. The UAVSAR pod flies on a NASA Gulfstream-III aircraft and is attached just below the wings. The aircraft flies at an altitude of 12.5 km to reduce interference from wind or moisture (Donnellan et al., 2018) B. A composite of two UAVSAR lines, collected in 2009 and 2010, showing the deformation caused the El Mayor Cucapah Earthquake. The image displays phase jumps corresponding to triggered fault slip in the study area. The CM scale displays how much slip occurred as seen from the radar. (Parker, 2019, Unpub. Data)

et al., 2018; Rockwell, 2016; Philibosian et al., 2011). Because this fault, and faults associated with HSFZ, cut pre-Holocene and unconsolidated materials, and the area is marked by active, very flashy alluvial processes, they have discontinuous fault scarps and, therefore, have not been mapped in enough detail (Jänecke et al, 2018). In flat lying areas, expression of the HSFZ is cryptic and researchers are forced to rely on vegetation lineaments, beheaded drainages, ephemeral ground cracks, or other surficial features which may or may not be actual expressions of this fault (Figure 4; Evans et al., 2018 Proposal; McNabb et al., 2017). At the northern end of the HSFZ, it is near vertical in the bedrock, and displays horizontal slickenlines (Bradbury, Evans, Jänecke, Unpublished data; Moser, 2017). Towards the south, the fault steps left exhibiting evidence of active ground deformation and may connect with the Hot Springs Fault to the east or the SAF in the west (Faherty et al., 2018; Evans et al., 2018 Proposal). Additionally, an active and migrating CO2 charged spring is currently endangering a major railroad and highway along a possible speculative southern continuation the of the fault zone (Lynch et al., 2018).

Methods

This study integrates modern and traditional remote sensing techniques with previous geologic maps, geologic field work, and structural analyses for the study area. I am creating a georeferenced integrated model of the fault zone, using ESRI's ArcMap combined with Google Earth Pro, that includes fault locations, orientations, geologic units, off-fault structures, and other fault associated features. Data for this study come from the NASA UAVSAR system, LiDAR data, examination of aerial photographs acquired from 1953 to 2018, and field-based observations.

UAVSAR

We use Uninhabited Aerial Vehicle Synthetic Aperture Radar (UAVSAR) and Interferometric Synthetic Aperture Radar (InSAR) datasets from collaborative work (Donnellan, 2018) to identify areas of active ground deformation east of the SSAF. InSAR uses two synthetic aperture images to create maps showing surface deformation. UAVSAR is NASA-JPL's aerial InSAR platform (Donnellan et al, 2018) in which data are acquired via a radar pod attached to a NASA-research plane (Figure 3) that flies repeated, high precision auto-piloted paths over an area. The UAVSAR pod sends radar signals to the surface of the earth (Donnellan et al., 2016, 2017). The transmitting signal from the aircraft towards the ground collects information based on the phase of the returned radiation, which is dependent on the distance to the ground. A radar pixel in these techniques corresponds to a surface extent of about 7 m, allowing for repeated high-resolution images of the surface to be created. A slight difference in the position of the aircraft for the two images allows the topography of a region to be revealed. When repeat flights are conducted over the same area, an interferogram can be created, highlighting the strain differences between the two images. Using precise autopilot to fly the plane allows for the flight paths to be identical within a 10-meter margin of error (Donnellan et al., 2016). The JPL-UAVSAR data for this region encompasses a decade of time, which is enough to have captured the effects of the 2010 El Mayor Cucapah, 2017 Chiapas, and 2019 Ridgecrest earthquakes on the study area (Figure 3).

By working with NASA-JPL scientists to analyze data acquired by these repeat flights along the SAF, we are able to determine if there were notable changes in the landscape that help us to better refine the location of faults associated with the HSFZ and eventually calculate slip rates. We know the study area to be geologically complicated with cross-cutting faults, and those signals are often unknowingly interpreted as noise in the UAVSAR data compared to the signals from much larger, targeted faults (Donnellan 2019 Pers. Comm.). This relationship indicates that geologic field work helps to inform our interpretations of UAVSAR data. This data is currently being

compiled for integration into the geolocated map. By iteratively working through these data sets with NASA-JPL I create much more accurate maps of the area than we could achieve individually. With the SSAF overdue for its next large earthquake (Fialko, 2007), the maps produced by this study will provide a baseline for how this landscape was creeping prior to the next event. This can help in our understanding of how slip is distributed in the area, how the region deforms in a large event, and how triggered slip from large events is accommodated by small displacement faults.

LiDAR

Light detection and ranging (LiDAR) is a method of creating precise, georeferenced, representations of the earth's surface by collecting dense elevation data. Similar to UAVSAR, the raw data for the LiDAR datasets we used were collected by attaching a sensor to a plane allowing it to collect a large amount of data in a relatively short amount of time. Extremely focused light pulses are sent to the surface of the earth and their travel time back to the sensor is recorded (NOAA, 2012). By calculating the distance between the sensor and the surface, extremely detailed and accurate images are created of the earths surface, showing details missed in coarser remote sensing methods.

LiDAR imagery was retrieved from Open Topography (USGS, 2012) and covers, roughly, the south west third of the outlined study area. This dataset was collected as part of the 2010 Salton Sea Lidar Collection project which obtained airborne lidar for the five kilometer radius around the shoreline of the Salton Sea. Data was collected in November when the inland sea is at its annual minimum water level. The resolution of the raster produced is 1 meter and has a vertical accuracy of 9.25 centimeters.

Image Analysis

We use satellite and aerial imagery acquired over a time span of 30, and 60, years, respectively, to identify visible traces of the HSFZ, and the faults in the immediate vicinity, by looking for certain fault related features. These features include the obvious ground fractures and offset patterns visible but more commonly include beheaded streams, influenced drainages, springs, oases, and vegetation lineaments (Figures 4 and 5). While the latter features do not give us any absolute displacements, they are important indicators to most likely locations of minor faults. Field work to ground truth these minor faults was originally scheduled for spring 2020 has been cancelled due to the Covid-19 pandemic and likely will not take place for this project. Thus, an important component of this work will be to produce maps of the region to guide further field-based research.

Features are being mapped at a variety of scales. Imagery provided by, and available only through, Google Earth Pro yields the most fine scaled mapping, exclusively for 2015, with a resolution of roughly 10 cm. This impressive resolution allows us to discern features otherwise obscured by the coarser resolution of NAIP and satellite imagery, such as ground cracks formed in response to faulting, as well as minor drainages

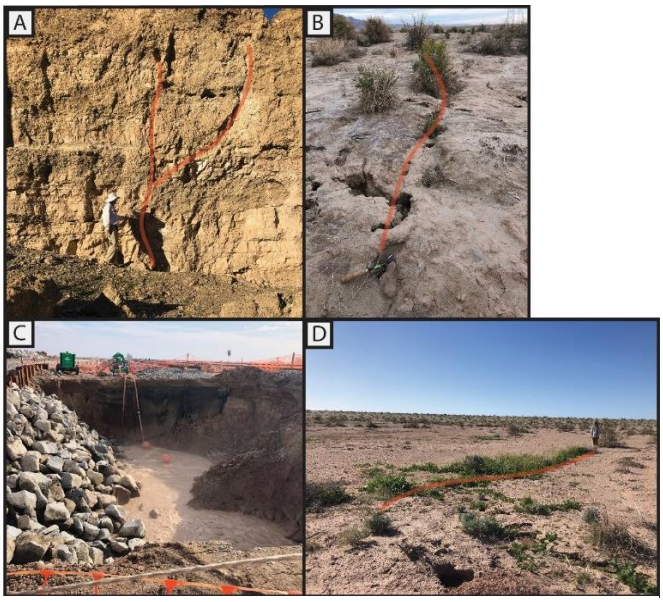

Figure 4. Expressions of faulting in the HSFZ. Locations of these features are shown in Figure 2 with corresponding letters. **A.** Faulting and offset **B.** Ground cracks **C.** CO_2 charged spring which is affecting the railways **D.** vegetation lineament

and small fault scarps. The three-dimensional capabilities of Google Earth Pro have proven to be helpful in certain regions of the study area, allowing us to view faults in canyon outcrops and in some cases to determine the sense of slip on a fault.

Images from the National Agriculture Imagery Program (NAIP) were retrieved from Earth Explorer (USDA, 2019) on January 8, 2020. NAIP imagery was selected for this project because of its temporal distribution, number of bands, and pixel size. Specific Images were selected based on their immediate proximity to the outlined study area and represent an area of roughly 40 km2 each. All images were collected in July and August, those months were selected as they are the driest for the region. Four banded images containing red, green, blue and near infrared bands were available for 2012, 2014, 2016, and 2018. Three banded images, omitting the near infrared band, were available for 2005, 2009 and 2010. The pixel size for the four banded images is 0.6 m x 0.6 m, and for the three banded images is 1 m x 1m. Between 20 and 23 images spanning the study area were downloaded for each year, although not all images will be used in their entirety.

Using a Python3 (Rossum and Drake, 2009) script each image was processed and organized. For each downloaded image a natural color image (band order: red, green, blue) was created as well as an enhanced contrast image created by applying a histogram stretch to the natural color image. Two false color images were also generated per file. The false color images were generating by applying a histogram stretch to a temporary false color raster, the resulting file was exported. False color histogram stretch images were created using 142 (red, near infrared, green) and 423 (near infrared, green, blue) band combinations. These combinations were selected because they created the most spectrally diverse images which highlight vegetation, water and created a greater differentiation between rock units. All resulting images are georeferenced and projected in NAD83 UTM Zone 11N.

Historical imagery was downloaded from the University of California, Santa Barbara online aerial image library for the year 1953 (USDA, 1953). This imagery was collected using panchromatic film and is available at a 1: 63,360 scale. These images were georeferenced in ArcMap and projected to NAD83 UTM Zone 11N. Because of the nature of the images the georeferencing is imperfect, edges are distorted, and some features are offset from their actual ground expression. Additionally, because of the lack of distinguishing permanent features in the study area typically used in georeferencing (roads, water towers, buildings, etc.) and because the landscape has changed in the last 60 years, some of the images' georeferencing relied on previous historic images, further reducing their accuracy on the ground. Despite the complications with historical imagery, the images are still valuable. Drainage patterns have changed in certain areas since 1953 and this vintage of data allows us to see fault related features such as beheaded streams and influenced drainages that have since been obscured.

An important complication to mention with this type of imagery is the influence of anthropomorphic forces on the landscape. A few new roads and neighborhoods have been constructed since the 1953 images were collected, distorting ground features. Additionally, increased usage of off-highway vehicles (OHVs) in the past ~20 years in this desert has distorted fault features, altered drainage patterns, and affected vegetation. The effects of these vehicles are seen not only in the aerial images, but also in LIDAR data.

Outcomes to Date

The nature of the faults in the study area is expressed slightly differently in different regions. To best cover these trends, I discuss the study area in three sections: Southeast, Central, and Northwest.

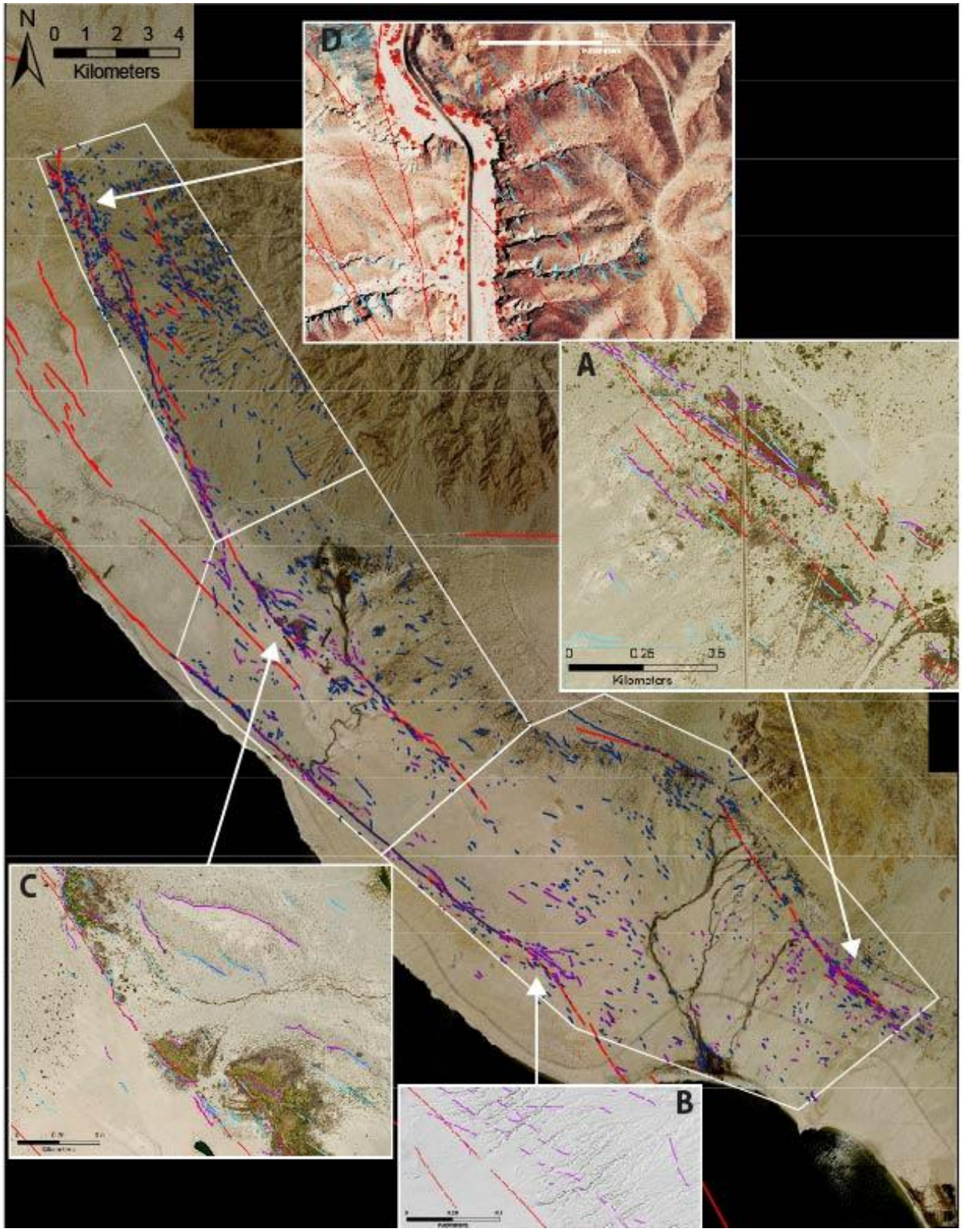

Figure 5. This figure shows the defined outline of the study area (white) over a NAIP image from 2016. Red lines indicate known faults from the Quaternary Fault and Fold Database (Bryant, 2005; USDA, 2019), purple lines are faults identified in this study based on LiDAR imagery (USGS, 2012), blue lines are faults identified by this study based on NAIP imagery. **A.** Vegetation lineaments shown on natural color NAIP imagery **B.** Beheaded streams shown on LiDAR **C.** Oases shown on natural color NAIP imagery **D.** Fault scarps and physical offset shown on false color NAIP imagery.

Southeast

The Southeast portion of the study area is bound by the Coachella Canal to the east and Bombay Beach, the Salton Sea, and highway 111 to the south. A number of small neighborhoods, RV parks and artificial lakes are scattered in this region. Nearly parallel to the Coachella Canal is the main trace of the HoSF, trending NNW/SSE (Figure 5A) A large drainage system trends southwest and then switches to southeast as it flows to the Salton Sea. In the region east of this drainage, I mapped a large number of faults striking nearly parallel to the HoSF main trace. These faults were almost entirely characterized by the presence of vegetation lineaments. The use of false color imagery in this area was particularly helpful as substituting NIR for the red band highlights the presence of healthy vegetation. The false color imagery also made it easier to differentiate different rock and soil types. LiDAR data was helpful in identifying drainages affected by faulting that were ill defined in the aerial images as well as several fault scarps not visible. These newly identified faults mark a zone of deformation approximately one kilometer wide on either side of the main HoSF.

To the west of the large drainage, faults are characterized by the particularly angular portions of drainages, beheaded drainages, and visible physical offset (Figure 5B). These faults trend largely NW/SE, consistent with the general trend of faults in this region, despite no significant master faults in the immediate vicinity. On the southeastern edge of this region is the SSAF trending NW/SE. Almost all newly identified faults in the one-kilometer wide deformation zone parallel the SSAF. This region is also marked by a number of beheaded streams, tight folding and angular unconformities. There are a few fault scarps visible as well in both the aerial imagery and LiDAR.

Central

The central portion of the study area is marked by the large, meandering Salt Creek, and the presence of the southern portion of the HSFZ in its center (Figure 5C). The southwestern portion of this region is bound by highway 111 and the SSAF, the north east potion is characterized by the presence of a large alluvial fan and the foothills of the Orocopia Mountains. The total zone of deformation in this region is roughly eight kilometers wide, encompassing the SSAF, the Mecca Fault, and the HSFZ. The HSFZ and SSAF appear to have the largest influence on the trend of the newly identified faults in this area. Faults immediately near the SSAF parallel it and trend NW/SE. Faults in the HSFZ largely trend NNW/SSE with the main fault. Newly identified faults are largely marked by beheaded streams and other drainages influenced by faulting, as well as vegetation lineaments. These lineaments are particularly noticeable towards the head of Salt Creek and nearby the 5-6 large oases. Physical offset can be observed in regions closest to the SSAF as well as one area where exposed bedding is faulted several times near one oasis. Tight folding and angular unconformities are once again visible to the south west, parallel to the SSAF. While the pattern of Salt Creek has changed since the 1953 imagery, most of the features indicative of faulting are observed in both the 1953 and recent images. These features, along with several fault scarps, are also visible in the LiDAR imagery of the area.

Northwest

The northern most portion of the study area is significantly different than the previous two thirds. This region is marked by the Orocopia Mountains to the east, and the foothills of the Mecca Hills to the west. This region is almost entirely influenced by the HSFZ in the Mecca Hills, although significant deformation has been mapped in the through the entire 4.5 kilometer width of the area. New faults trend mostly parallel to the HSFZ trending largely NW/SE. A few of these many faults were identified by plant lineaments or beheaded drainages, however, the vast majority were identified by fault scarps, physical offset, and unconformities (Figure 5D). In some regions differentiating between

geomorphic processes and faulting was difficult. Mapping of this region is largely aided by the three-dimensional capabilities of Google Earth Pro, by allowing us to get a closer look at features to determine if there is offset on observed scarps, or to trace the observed faults onto their outcrops. Additionally, Google Earth's Street view has been helpful at times, although sometimes distorted by the low angle of the sun on the date of collection, in identifying faults and offset in outcrops.

Conclusions

The newly identified faults provide strong evidence for a wider and more populated fault zone than currently mapped. While we are currently unable to visit the field area to look for physical evidence of offset, the addition of UAVSAR data to our current map will potentially reveal regions of slip that could be confirmed later. The maps resulting from this research will help to fill in the gaps of what is known about the fault patterns of this region and will hopefully be a resource in guiding future studies on this area.

Acknowledgements

This research was made possible by the support from my thesis committee: James Evans, Susanne Jänecke and Andrea Donnellan as well as the data being shared by Dr. Donnellan and Jay Parker from NASA-JPL. I also want to thank Kelly Bradbury and Amy Moser for allowing us to use their unpublished data from the region. Finally, this project is funded by the UNSGC, GSA, and the USU Geoscience Department.

References

Axen, G.J., and Fletcher, J.M., 1998, Late Miocene-Pleistocene extensional faulting, northern Gulf of California, Mexico and Salton Trough, California: International Geology Review, v. 40, p. 217–244, doi:10.1080/00206819809465207.

Babcock, E.A., 1974, Geology of the Northeast Margin of the Salton trough, Salton Sea, California: Bulletin of the Geological Society of America, v. 85, p. 321–332, doi:10.1130/0016- 7606(1974)85<321:GOTNMO>2.0.CO;2.

Bryant, W. A. (compiler), 2005, Digital Database of Quaternary and Younger Faults from the Fault Activity Map of California, version 2.0: California Geological Survey Web Page, <http://www.consrv.ca.gov/CGS/information/publications/QuaternaryFaults_ver2.htm>; (accessed: 6/1/2019)

Cheng, Y., Ross, Z.E., and Ben-Zion, Y., 2018, Diverse Volumetric Faulting Patterns in the San Jacinto Fault Zone: Journal of Geophysical Research: Solid Earth, v. 123, p. 5068–5081, doi:10.1029/2017JB015408.

Crowell, J.C., and Susuki, T., 1959, Eocene stratigraphy and paleontology, Orocopia Mountains, southeastern California: Bulletin of the Geological Society of America, v. 70, p. 581–592, doi:10.1130/0016-7606(1959)70[581:ESAPOM]2.0.CO;2

DeMets, C., Gordon, R.G., and Argus, D.F., 2010, Geologically current plate motions: Geophysical Journal International, v. 181, p. 1–80, doi:10.1111/j.1365-246X.2009.04491.x.

DeMets, C., and Merkouriev, S., 2016, High-resolution reconstructions of Pacific-North America plate motion: 20 Ma to present: Geophysical Journal International, v. 207, p. 741–773, doi:10.1093/gji/ggw305.

Dibblee, T.W., 1954, Geology of the Imperial Valley region, California: in: Jahns, R. H., ed., Geology of southern California, California Division of Mines and Geology Bulletin, v. 170, p. 21–28.

Donnellan, A., Arrowsmith, R., and DeLong, S., 2017, Spatio-Temporal Mapping of Plate Boundary Faults in California Using Geodetic Imaging: Geosciences, v. 7, p. 15, doi:10.3390/geosciences7010015.

Donnellan, A., Parker, J., Granat, R., Glasscoe, M., Lyzenga, G., Pierce, M., Wang, J., Ma, Y., Ludwig, L., and Rundle, J., 2016, Uninhabited Aerial Vehicle Synthetic Aperture Radar Observation of Recent Earthquakes in California: NASA-Jet Propulsion Lab, https://trs.jpl.nasa.gov/handle/2014/46016.

Donnellan, A., Parker, J., Heflin, M., Lyzenga, G., Moore, A., Ludwig, L.G., Rundle, J., Wang, J., and Pierce, M., 2018, Fracture Advancing Step Tectonics Observed in the Yuha Desert and Ocotillo, CA, Following the 2010 Mw7.2 El Mayor-Cucapah Earthquake: Earth and Space Science, v. 5, p. 456–472, doi:10.1029/2017EA000351.

Dorsey, R.J., and Umhoefer, P.J., 2012, Influence of Sediment Input and Plate-Motion Obliquity on Basin Development Along an Active Oblique-Divergent Plate Boundary: Gulf of California and Salton Trough, in Tectonics of Sedimentary Basins: Recent Advances, p. 209–225, doi:10.1002/9781444347166.ch10.

ESRI, ArcGIS ArcMap 10.7.1, 2019, ESRI Inc., Redlands, CA.

Evans, E.L., 2018, A comprehensive analysis of geodetic slip-rate estimates and uncertainties in California: Bulletin of the Seismological Society of America, v. 108, p. 1–18, doi:10.1785/0120170159.

Evans, E.L., Thatcher, W.R., Pollitz, F.F., and Murray, J.R., 2016, Persistent slip rate discrepancies in the eastern California (USA) shear zone: Geology, v. 44, p. 691–694, doi:10.1130/G37967.1.

Evans, E.L., Loveless, J.P., and Meade, B.J., 2015, Total variation regularization of geodetically and geologically constrained block models for the Western United States: Geophysical Journal International Geophys. J. Int, v. 202, p. 713–727, doi:10.1093/gji/ggv164.

Faherty, D., and Polet, J., 2018, Geophysical investigation of fault-groundwater interaction: San Andreas Oasis site study, in Technical Program Expanded Abstracts, p. 246–2500.

Fattaruso, L.A., Cooke, M.L., Dorsey, R.J., and Housen, B.A., 2016, Response of deformation patterns to reorganization of the southern San Andreas fault system since ca. 1.5 Ma:

Tectonophysics, v. 693, p. 474– 488, doi:10.1016/j.tecto.2016.05.035.

Fialko, Y., 2006, Interseismic strain accumulation and the earthquake potential on the southern San Andreas fault system: Nature, v. 441, p. 968–971, doi:10.1038/nature04797.

Field, E.H. et al., 2013, The Uniform California Earthquake Rupture Forecast, Version 3 (UCERF3)-The Time-Independent Model: U.S. Geological survey Open-file Report 2013-1165, v. 97, https://pubs.usgs.gov/of/2013/1165/pdf/ofr2013-1165.pdf (accessed February 2019).

Google, Earth Pro, 2020. Earth.google.com

Hauksson, E., Meier, M., Ross, Z.E., and Jones, L.M., 2017, Evolution of seismicity near the southernmost terminus of the San Andreas Fault: Implications of recent earthquake clusters for earthquake risk in southern California: Geophysical Research Letters, v. 44, p. 1293–1301, doi:10.1002/2016GL072026.

Hays, W. H. Geology of the central Mecca Hills, Riverside County, California: Yale University, New Haven, Connecticut, unpublished Ph. D. Diss. thesis, 324 p., map scale 1: 14,000, 1957.

Jänecke, S.U., Markowski, D.K., Evans, J.P., Persaud, P., and Kenney, M., 2018, Durmid ladder structure and its implications for the nucleation sites of the next M > 7.5 earthquake on the San Andreas fault or Brawley seismic zone in southern California: Lithosphere, v. 10, p. 602–631, doi:10.1130/L629.1.

Janecke, S., Dorsey, B., and Belgarde, B., 2010, Age and Structure of the San Jacinto and San Felipe fault zones, and their lifetime slip rates, in Clifton, H.E. and Ingersoll, R.V. eds., Geologic Excursions in California and Nevada: tectonics, stratigraphy, and hydrogeology, SEPM (Society for Sedimentary Geology), p. 233–271, http://pages.uoregon.edu/rdorsey/Downloads/JaneckeEtal2010FT.pdf (accessed February 2018).

Jennings, C.W., compiler, 1977, Geologic map of California: California Division of Mines and Geology Geologic Data Map 2, scale 1:750,000.

Kirby, S.M., Janecke, S.U., Dorsey, R.J., Housen, B.A., Langenheim, V.E., McDougall, K.A., and Steely, A.N., 2007, Pleistocene Brawley and Ocotillo formations: Evidence for initial strike-slip deformation along the San Felipe and San Jacinto fault zones, southern California: Journal of Geology, v. 115, p. 42–62, doi:10.1086/509248.

Kyriakopoulos, C., Oglesby, D.D., Rockwell, T.K., Meltzner, A.J., Barall, M., Fletcher, J.M., and Tulanowski, D., 2019, Dynamic Rupture Scenarios in the Brawley Seismic Zone, Salton Trough, Southern California: Journal of Geophysical Research: Solid Earth, v. 124, p. 3680–3707, doi:10.1029/2018JB016795.

Lin, J., and Stein, R.S., 2004, Stress triggering in thrust and subduction earthquakes and stress interaction between the southern San Andreas and nearby thrust and strike-slip faults: Journal of Geophysical Research: Solid Earth, v. 109, p. 1–19, doi:10.1029/2003jb002607.

Lindsey, E.O., and Fialko, Y., 2013, Geodetic slip rates in the southern San Andreas Fault system: Effects of elastic heterogeneity and fault geometry: Journal of Geophysical Research: Solid Earth, v. 118, p. 689–697, doi:10.1029/2012JB009358.

Lindsey, E.O., Fialko, Y., Bock, Y., Sandwell, D.T., and Bilham, R., 2014, Localized and distributed creep along the southern San Andreas Fault: Journal of Geophysical Research : Solid Earth, v. 119, p. 7909–7922, doi:10.1002/2014JB011275.1.

Lisowski, M., Savage, J.C., and Prescott, W.H., 1991, The velocity field along the San Andreas Fault in central and southern California: Journal of Geophysical Research, v. 96, p. 8369–8389, doi:10.1029/91JB00199.

Lundgren, P., Hetland, E.A., Liu, Z., and Fielding, E.J., 2009, Southern San Andreas-San Jacinto fault system slip rates estimated from earthquake cycle models constrained by GPS and interferometric synthetic aperture radar observations: Journal of Geophysical Research: Solid Earth, v. 114, p. 1–18, doi:10.1029/2008JB005996.

Lutz, A.T., 2005, Tectonic controls on Pleistocene basin evolution in the central San Jacinto fault zone, southern California, [M.S. thesis]: Eugene, University of Oregon, 136 p.

Lutz, A.T., Dorsey, R.J., Housen, B.A., and Janecke, S.U., 2006, Stratigraphic record of Pleistocene faulting and basin evolution in the Borrego Badlands, San Jacinto fault zone, Southern California: Bulletin of the Geological Society of America, v. 118, p. 1377–1397, doi:10.1130/B25946.1.

Lynch, D. K., Deane, T., Zamora, C., Francuch, D. G., Bailey, J. S., Allen, C. W., Rogers, J. D., & Gouger, C., 2018. A Moving Mud Pot Threatening Railroad Tracks and a Highway, Imperial County, California. Poster Presentation at 2018 SCEC Annual Meeting.

Markowski, D.K., 2016, Confirmation of a New Geometric and Kinematic Model of the San Andreas Fault at Its Southern Tip, Durmid Hill, Southern California: Utah State University, https://digitalcommons.usu.edu/etd/4987 (accessed August 2019).

Mcnabb, J. C., Dorsey, R. J., Housen, B. A., Dimitroff, C. W., & Messé, G. T. (2017). Stratigraphic record of Pliocene-Pleistocene basin evolution and deformation within the Southern San Andreas Fault Zone, Mecca Hills, California. Tectonophysics, 719–720, 66–85. https://doi.org/10.1016/j.tecto.2017.03.021

Moser, A., 2017, Spatiotemporal Evolution of Pleistocene and Late Oligocene-Early Miocene Deformation in the Mecca Hills, Southernmost San Andreas Fault Zone: Utah State University.

Moser, A.C., Evans, J.P., Ault, A.K., Janecke, S.U., and Bradbury, K.K., 2017, (U–Th)/He thermochronometry reveals Pleistocene punctuated deformation and synkinematic hematite mineralization in the Mecca Hills, southernmost San Andreas Fault zone: Earth and Planetary Science Letters, v. 476, p. 87–99, doi:10.1016/j.epsl.2017.07.039.

National Oceanic and Atmospheric Administration (NOAA) Coastal Services Center. 2012. “Lidar 101: An Introduction to Lidar Technology, Data, and Applications.” Revised. Charleston, SC: NOAA Coastal Services Center.

Petersen, M.D. et al., 2014, Documentation for the 2014 Update of the United States National Seismic Hazard Maps: U.S. Geological Survey Open-File Report, p. 243 p., doi:http://dx.doi.org/10.3133/ofr20141091.

Philibosian B., Fumal T., and Weldon R., 2011, San Andreas fault earthquake chronology and Lake Cahuilla history at Coachella, California: Seismological Society of America Bulletin, v. 101, p. 13–38, https://doi.org/10.1785/0120100050.

Polet, J., Tyagi, A. and R. Ng, 2019, Ambient Noise Spectral Ratio Analysis of High Density Seismic Deployments Across Several Southern California Sedimentary Basins, Paper in the

Proceedings of 2nd International Conference on Natural Hazards & Infrastructure, Chania, Greece, 10 pp.

Rockwell, T., 2016, Open intervals, clusters and supercycles: 1100 years of Moment release in the southern San Andreas Fault system: Are we ready for the century of earthquakes?: Southern California Earthquake Center, https:// les.scec.org/s3fs-public/publication_6367. pdf (accessed 26 April 2018).

Roten, D., Olsen, K.B., Day, S.M., Cui, Y., and Fäh, D., 2014, Expected seismic shaking in Los Angeles reduced by San Andreas fault zone plasticity: Geophysical Research Letters, v. 41, p. 2769–2777, doi:10.1002/2014GL059411.

Roten, D., Olsen, K.B., and Day, S.M., 2017, Off-fault deformations and shallow slip deficit from dynamic rupture simulations with fault zone plasticity: Geophysical Research Letters, v. 44, p. 7733–7742, doi:10.1002/2017GL074323.

Spinler, J.C., Bennett, R.A., Anderson, M.L., McGill, S.F., Hreinsdóttir, S., and McCallister, A., 2010, Present-day strain accumulation and slip rates associated with southern San Andreas and eastern California shear zone faults: Journal of Geophysical Research: Solid Earth, v. 115, doi:10.1029/2010JB007424.

Steely, A.N., Janecke, S.U., Dorsey, R.J., and Axen, G.J., 2009, Early Pleistocene initiation of the San Felipe fault zone, SW Salton Trough, during reorganization of the San Andreas fault system: Bulletin of the Geological Society of America, v. 121, p. 663–687, doi:10.1130/B26239.1.

Thatcher, W., Savage, J.C., and Simpson, R.W., 2016, The Eastern California Shear Zone as the northward extension of the southern San Andreas Fault: Journal of Geophysical Research: Solid Earth, v. 121, p. 2904–2914, doi:10.1002/2015JB012678.

Tong, X., Sandwell, D.T., and Smith-Konter, B., 2013, High-resolution interseismic velocity data along the San Andreas Fault from GPS and InSAR: Journal of Geophysical Research: Solid Earth, v. 118, p. 369–389, doi:10.1029/2012JB009442.

Tong, X., Sandwell, D., and Smith-Konter, B., 2012, A systematic estimation of fault creep rates along major faults in California from L-band radar interferometry, in 2012 Annual Meeting of Southern California Earthquake Center, Univ. Southern California/ Southern California Earthquake Center, Palm Springs, CA, p. 205.

USDA-FSA-APFO Aerial Photography Field Office. 2019. National Geospatial Data Asset (NGDA) NAIP Imagery. Accessed January 8, 2020.

USDA, 1953, Aerial Imagery of the Salton Sea, CA: University of California , https://www.library.ucsb.edu/src/collections-aerial-photography (accessed 2020).

U.S. Geological Survey and California Geological Survey, 2006, Quaternary fault and fold database for the United States, accessed December 4, 2019, from USGS web site: http//earthquake.usgs.gov/hazards/qfaults/

U.S. Geologic Survey, 2012, 2010 Salton Sea LiDAR Collection. https://doi.org/https://doi.org/10.5069/G9V985ZF.